Progress in Propulsion Physics **11** (2019) 529-542
https://doi.org/10.1051/eucass/201911529

SHALLOW WATER EXPERIMENTS TO VERIFY A NUMERICAL ANALYSIS ON AN AERODYNAMICALLY THRUST-VECTORED AEROSPIKE NOZZLE

J. Sieder, M. Propst, C. Bach, and M. Tajmar

Technische Universität Dresden
Institute of Aerospace Engineering
Dresden 01062, Germany

Shallow water experiments are predestined for fast and inexpensive experimental examination of two-dimensional (2D) flow phenomena. In this study, the shallow water analogy is used for the verification of a previous numerical analysis of an aerodynamically thrust-vectored aerospike nozzle. Experiments in a shallow water channel were conducted, using a model of an isentropic spike with a 25 percent truncation and two secondary injection sites. A comparison of the flow phenomena, e. g., shock patterns, shows a wide correspondence of experimental and simulation results, thus verifying the simulation approach and encouraging to continue its improvement. Furthermore, it can be shown that secondary fluid injection is a promising method for active thrust vectoring on aerospike thrusters and gives an objective for future applications.

1 INTRODUCTION

Aerospike or plug nozzle engines have been developed and tested since the 1950s as an alternative to classical bell nozzles [1–12]. With their advantageous performance characteristics during the ascent, they have been considered for the upper stage of Saturn V and the Space Shuttle Main Engine [13]. During the 1990s, linear plug nozzle engines were the single-stage-to-orbit propulsion system of choice for the X-33 Mission also known as Venture Star.

Today, well known for their altitude adaptive characteristics up to the designed pressure ratio, this nozzle type is regaining the focus of interest. Besides further advantageous performance characteristics towards comparable bell nozzles, aerospike nozzles provide additional capability of active aerodynamic thrust vectoring. As demonstrated in cold gas flow tests [13, 14], aerodynamic thrust

vectoring provides side force control without mechanical devices, such as gimbals or flaps.

A numerical simulation has been conducted for a parametric analysis concerning thrust vectoring [15]. For the verification of the observed flow phenomena, a direct measurement of the hot gas flow is hardly feasible. The analogy of incompressible liquid flows with free surfaces on one side and compressible gas flows on the other side allows the examination of these flow phenomena in a shallow water channel for the first approximation. Besides the better accessibility of field quantities, a better visibility and smaller fluctuation frequencies due to a time scaling effect allow a qualitative analysis of the stream behavior [16].

Within this paper, an experimental flow phenomena analysis concerning aerodynamic thrust vectoring on aerospike nozzles is presented. It starts with the description of the function principle of aerospike nozzles and thrust vectoring in section 2. In section 3, the underlying relation of hot gas supersonic flows and shallow water surface waves for the shallow water analogy is summarized. From the nozzle geometry used for the computational fluid dynamics (CFD) simulations, the manufactured water model is derived. Furthermore, this section describes the utilized test bench. The obtained results from the experiments are presented and discussed in section 4. Finally, the flow phenomena are compared with previous CFD-calculation results.

2 AEROSPIKE AND THRUST-VECTORING CONCEPTS

Aerospike nozzles can be classified into linear and annular plug nozzle designs. Both offer the possibility of having a single or a clustered combustion chamber arrangement. The clustered combustion chamber design inherently offers thrust-vectoring by applying the method of differential throttling of single chambers. Furthermore, it offers a design choice between fully external or partial internal expansion of the exhaust gases by adding an additional divergent nozzle structure behind the nozzle throat [3, 4]. The method of differential throttling proposes suitable thrust-vectoring for medium and high thrust rocket engines. Nevertheless, it is not applicable for smaller rocket engines with a single annular combustion chamber. In that case, aerodynamic thrust vectoring is a promising method for side-force generation in order to steer a rocket or satellite. The injection of a secondary fluid with a high radial flow component into the axial supersonic main exhaust flow results in a deflection of the latter. This deflection creates an additional side-force component to the inherent thrust of secondary fluid flow. Figure 1 shows the Mach number distribution in which the function principle of aerodynamic thrust-vectoring is visible. The interaction of the secondary flow with the main flow causes a bow shock, resulting in an asymmetric flow and, consequently, pressure distribution around the aerospike nozzle.

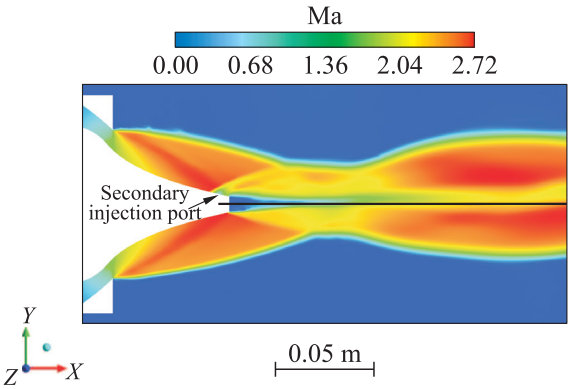

Figure 1 Local Mach number distribution for a thrust-vectored aerospike flow [15]

Due to high thermal loads at the nozzle exit as well as aspects of weight optimization and difficulties in manufacturing sharp edges, an ideal isentropic spike usually gets truncated. This truncation is always bound to losses according to the nozzle performance [3]. Additionally, plug nozzles offer various advantages for exo-atmospheric flight missions. Because of their shape, plug nozzles can reach greater expansion ratios and, therefore, a higher specific impulse while having the same footprint size with regard to bell nozzles. The cooling of aerospike nozzles is one of their major disadvantages [17].

3 EXPERIMENTAL SETUP

A brief summary of the shallow water analogy is presented, followed by a description of the utilized test bed and the nozzle model.

3.1 Shallow Water Analogy

For examinations using analogies, a physical process (original) is studied based on the second process (model) which can be described with the same mathematical correlations (field quantities, boundary and initial conditions). The geometry of the model needs to be equal or similar to the original one.

The analogy of shallow water waves (wave length $\geq 20h_W$) and 2D gas streams can be derived by using energy and mass conservation equations for both fluids. The evaluation of this set of equations delivers a relation between the water height h_W in the shallow water channel and the corresponding gas parameters: temperature T, density ρ, and pressure p. The parameter

Table 1 Parameter relation [16]

Gas ($\kappa = 2$)	Shallow water
T/T_0	$h_W/h_{W,0}$
ρ/ρ_0	$h_W/h_{W,0}$
p/p_0	$(h_W/h_{W,0})^2$
a	$c = \sqrt{g\,h_W}$
Ma	Fr

relations between these two flow models are summarized in Table 1 (index 0 indicates the fluid state at rest) [16, 18].

It is important to note that this analogy is exact only for gas flows with an isentropic exponent of $\kappa = 2$. Therefore, this analogy is used rather for qualitative than for absolute quantitative evaluation in the present case. Furthermore, a correspondence between sonic velocity a and traveling speed of surface waves $c = (g\,h_W)^{1/2}$ (g is the gravity constant) can be found. The Froude number (Fr $= w/c$, w is the local water speed) can be used correspondingly to the Mach number Ma to classify the flow:

$$\begin{aligned} &\text{Ma} < 1 : \text{subsonic gas flow} && \Longleftrightarrow && \text{Fr} < 1 : \text{subcritical water flow;} \\ &\text{Ma} = 1 : \text{sonic/choked gas flow} && \Longleftrightarrow && \text{Fr} = 1 : \text{critical water flow;} \\ &\text{Ma} > 1 : \text{supersonic gas flow} && \Longleftrightarrow && \text{Fr} > 1 : \text{supercritical water flow.} \end{aligned}$$

3.2 Test Bed — Shallow Water Channel

For the realization of the experiments, the shallow water channel of the Institute of Fluid Mechanics at the TU Dresden has been used. This test bed was designed in 1976 to visualize fluid flows [19]. A setup scheme of the test bed is shown in Fig. 2.

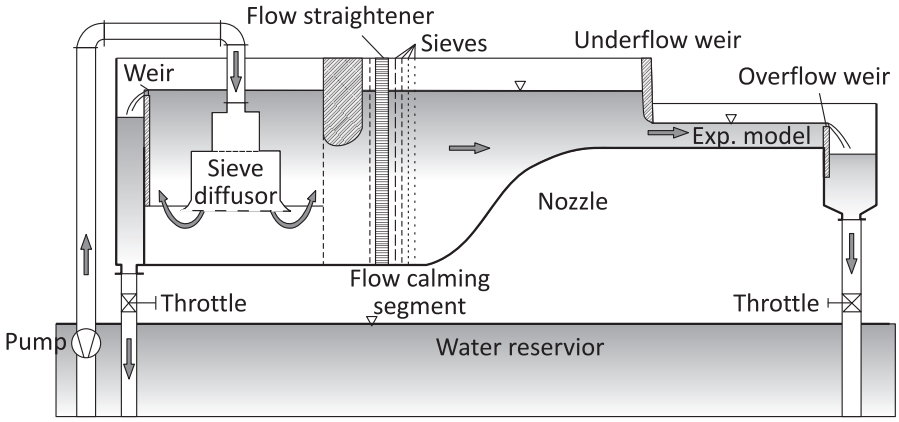

Figure 2 Shallow water test bed [19]

This test bed can be used for models with a footprint up to 1500×1000 mm and a height up to 200 mm. The applied nozzle model uses almost the complete base area of the experimental test bay. A volume flow up to 350 m^3/h is realized with a 15-kilowatt pump. The water height can be determined manually with a traversing unit. A vertically adjustable dipstick is then used to measure the height. For the measurement on a single data point, the dipstick is lowered from above until it barely touches the water surface. The local water height is obtained from a vernier scale on the dip stick adjusting mechanism. The last tenths of millimeters are usually overcome by the water surface tension, resulting in a measurement accuracy of around ± 1 mm.

To ensure consistent measurements, the water flow has to enter the model stationary, uniformly, parallel, and without fluctuations. For this purpose, several components were added to the test bed: the sieve diffuser throttles the flow in a short path without any separations which could cause fluctuations. Sieves and a flow straightener in the flow calming segment reduce residual flow rotations and large-scale fluctuations. The nozzle in front of the experimental model is used to accelerate the flow and to create a uniform velocity profile with a small boundary layer. The weirs can be used to ensure a stationary feeding water height in front of the test setup and, therefore, within the experimental model.

3.3 Nozzle Model

The contour of the annular full isentropic aerospike nozzle for a 3-kilonewton rocket engine has been determined with the FORTRAN code of C. C. Lee [1,20]. In this code, the simplification of a one-dimensional isentropic flow is used to calculate the nozzle contour via the area expansion ratio. The properties of the hot gases have been derived from the combustion of ethanol and liquid oxygen with a fuel mass ratio of 1:1. The same fuel combination is used in the SMART Rockets Project [21]; therefore, this nozzle could potentially be tested under real conditions at the TU Dresden. Table 2 lists the complete set of parameters for the nozzle design, delivering the spike contour shown in Fig. 3. During

Table 2 Design parameters for nozzle contour

Parameter	Value
Mach number at nozzle exit M_e	2.3
Expansion ratio (full spike) A_e/A_{throat}	2.941
Specific gas constant R_s	374.8 J/(kg·K)
Temperature at nozzle exit T_e	2024 K
Pressure ratio at nozzle exit p_e/p_0	1/15
Isentropic exponent κ	1.2

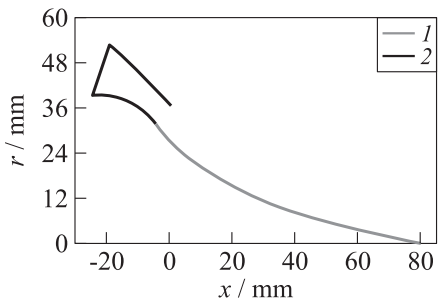

Figure 3 Contour of full isentropic aerospike nozzle (*1*) and combustion chamber (*2*) section

Figure 4 Nozzle within the shallow water channel

the 2D parameter study which was performed using CFD-analyses, a truncated spike with 75% of the full isentropic length has been chosen for further evaluation [15]. The main reasons for truncation are: less weight, improved cooling properties, and a better producibility of the spike (no sharp edges) while maintaining almost the flow pattern of the full isentropic spike. Within this study, the influence of the secondary injection position and variable mass flow rate on obtainable side forces and pressure distribution on the spike were investigated. The spike contour used in this parameter study serves as the basis for the development of the shallow water model (see also Fig. 3).

For reasons of better accessibility to measure the water surface, the nozzle for the shallow water channel has been scaled up by the factor of 5. First estimations showed that the primary diamond shaped high-pressure region contoured by the trailing shock should be well within the dimensions of the model. In order to realize the secondary injection, a water reservoir is implemented within the nozzle contour. Two 28-millimeter wide gate valves have been installed at 60% and 90% of the length of the remaining spike. The third gate valve is used upstream at the nozzle front to regulate the mass flow of water into this reservoir and, therefore, indirectly, the water height and pressure of the injection, respectively.

A set of inlet gaps provides an ambient flow simulating a working condition of the rocket engine traveling through the atmosphere. Two sieve rows are used to realize a more uniform ambient flow in axial direction. Additionally, two channels on each side of the model have been added to purge the major amount of water delivered by the test bench pump. This was necessary due to the limited adjustability of the water flow provided by the pump. For further possibilities of adjusting the water flow, one gate valve per channel has been included. The model within the channel is presented in Fig. 4.

4 EXPERIMENTAL RESULTS

Having defined the nozzle model to be tested and described the utilized shallow water channel, this section presents the results of the experiments. At first, the undisturbed flow around the center body of the aerospike nozzle is examined. Subsequently, the occurring flow phenomena are shown, including a measured surface height map. In the second subsection, the flow phenomena observed during flow deflection caused by secondary fluid injection are discussed.

4.1 Undisturbed Flow

Like bell nozzles, aerospike nozzles have a specific design pressure ratio p_e/p_0 at which they are fully adapted. This flow state is characterized by an exhaust flow parallel to the nozzle axis. In case of an overexpanded flow state, the working pressure ratio is above the design value and the downstream located exhaust flow bends towards the nozzle axis. For an underexpanded flow state, the working pressure ratio is below the design value and the gas flow bends away from the nozzle axis.

The aim of the first experiments was the reproduction of these three major flow states of expanding gases: overexpanded, adapted, and underexpanded. All of them can be created by adjusting the ambient flow and, thereby, ambient pressure by reducing/raising the ambient flow inlet cross section while keeping the combustion chamber at a constant predefined condition. A twine (indicated by an arrow in Fig. 5) has been used in the pictures to illustrate the free jet boundary. The usual method of adjusting the ambient pressure with the outflow weir could not be used, since the full open inlets of the ambient flow already created a water height resulting in an overexpanded nozzle flow.

For a comparison of the experimental results with the previously conducted simulations [22], the flow phenomena are identified in the latter according to the

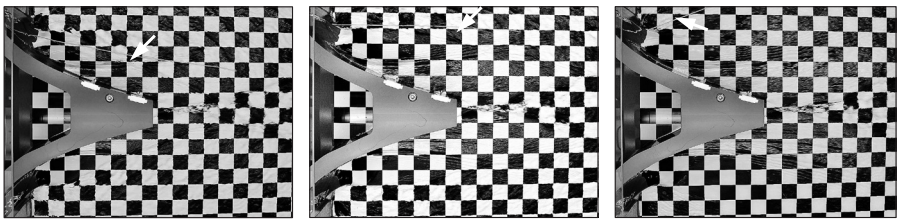

(*a*) (*b*) (*c*)

Figure 5 Nozzle flow states: (*a*) overexpanded; (*b*) adapted; and (*c*) underexpanded

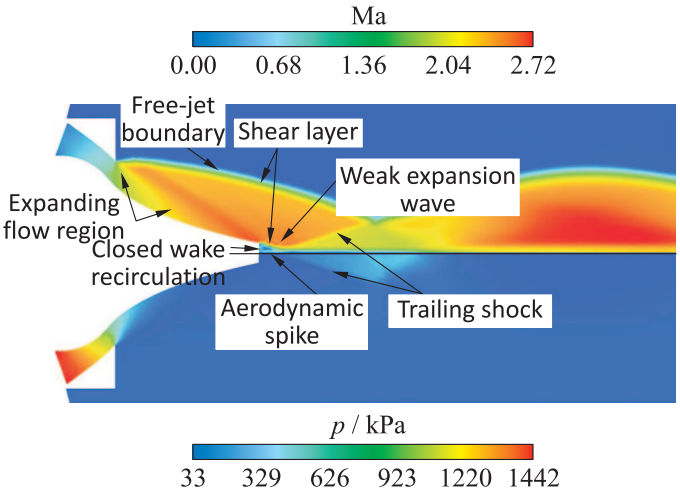

Figure 6 The CFD-result Mach number distribution (top) and static pressure distribution (bottom) [22]

work of Hall [23]. Figure 6 shows the location of all relevant flow phenomena for the overexpanded flow in a Mach number (top) and a static pressure distribution (bottom). It is obvious that most phenomena clearly visible in the Mach number plot are barely noticeable in the pressure plot. But as shown below, most of them are detectable on the photographs.

For the undisturbed, overexpanded flow condition, a water surface map has been measured manually for the interesting flow area using the traversing. With a horizontal and vertical resolution of 10 mm*, the map shown in Fig. 7 was obtained. During the measurement, the water height within the combustion chamber has been kept constant to 90 ± 4 mm. The height fluctuation is due to the lack of a fine adjustability of the water pump. These fluctuations at the inlet water height resulted in changes of the water surface below the water height measurement accuracy of ± 1 mm.

In this surface map, the expanding flow region and the trailing shock are clearly visible. The aerodynamic spike is visible through the dark blue area at the nozzle base. The weak expansion wave can be identified by the high gradient above the shear layer of the aerospike. The mentioned flow phenomena can be clearly identified in a photograph (Fig. 8). The surface map was not recalculated into a pressure map for hot gases due to the $\kappa = 2$ inaccuracy. Nevertheless, the flow phenomena of the conducted experiment and the numerical analyses correspond closely.

*Accuracy ± 1 mm; at the spike, a y-position error up to 2 mm was accepted.

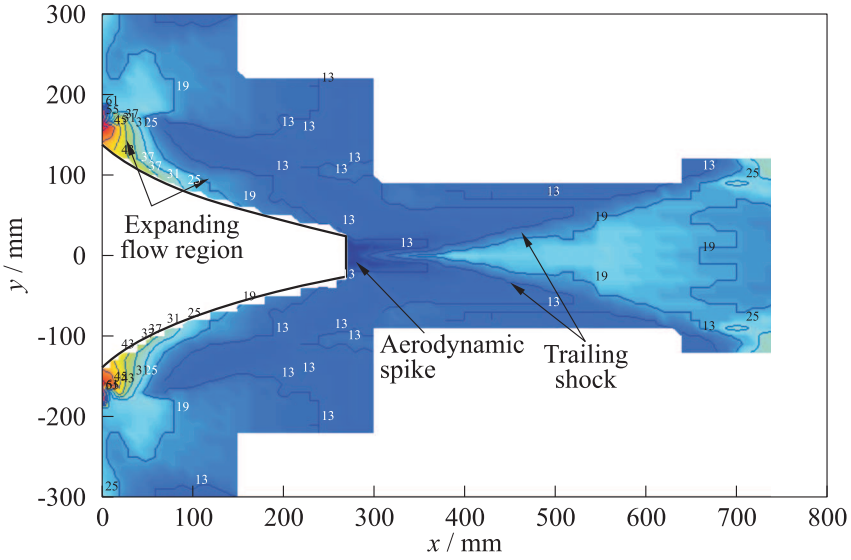

Figure 7 Water surface height map (indicating the gas flow static pressure by $p \sim h^2$)

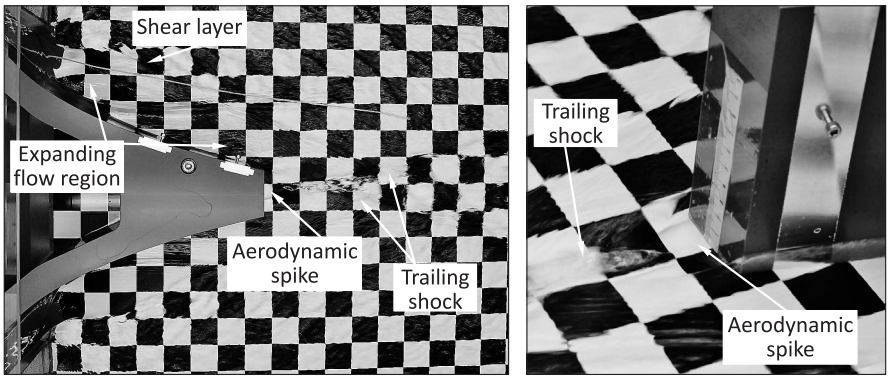

(*a*) (*b*)

Figure 8 Complete flow field (*a*) and aerospike base (*b*)

4.2 Deflected Flow

In this subsection, the flow phenomena which occur due to secondary injection are presented and discussed. This discussion is focused on an overexpanded main flow. To complete the survey on the conducted experiments, Fig. 9 shows the flow phenomena for adapted and underexpanded flows.

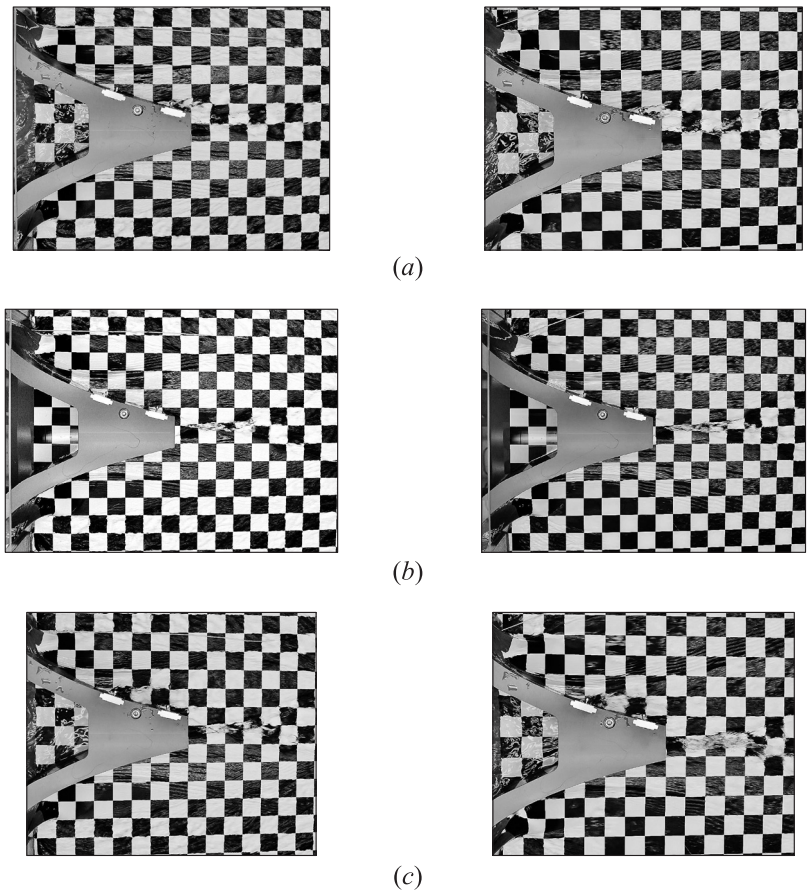

Figure 9 Adapted (left column) and underexpanded (right column) flows: (*a*) at 90 percent injection; (*b*) without injection; and (*c*) at 60 percent injection

Injection site at 90% of the spike length

When the secondary fluid is injected, a bow shock establishes towards the free-stream boundary (Figs. 10 and 11). This bow shock is accompanied by a region of higher pressure upstream the injection when compared to the undisturbed flow. This local pressure increase indicates a stagnation point at and a local subcritical flow upstream the injection site. Waidmann [24] discovered similar flow phenomena during the investigation of secondary injection in a supersonic flow within a conical nozzle. Furthermore, he identified an oblique shock on front of the injection site. Between oblique shock, nozzle wall, and secondary injection bow shock, he discovered a recirculation area. Such a recirculation area

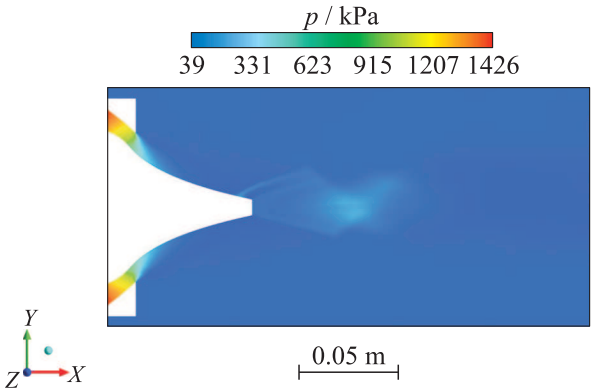

Figure 10 The CFD simulation: pressure distribution with 90 percent injection [22]

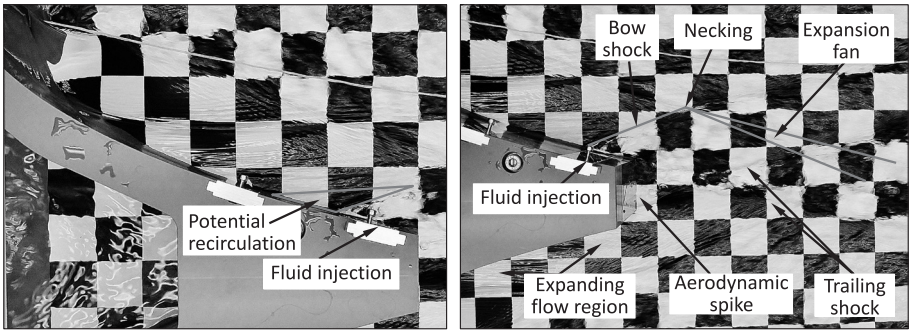

(*a*) (*b*)

Figure 11 Experiment: (*a*) recirculation area and (*b*) flow phenomena of an overexpanded flow with 90 percent injection

might have been observed in Figs. 10 and 11. Further downstream, the primary flow experiences a necking caused by the bow shock, which itself is reflected at the free-stream boundary towards the centralized compression shock behind the spike. This shock wave creates an expansion fan after the reflection, which is no longer verifiable at the downstream located region behind the first interference with the trailing shock.

Injection site at 60% of the spike length

When using the upstream located injection site, a similar bow shock appears like it is shown in the previous case (Figs. 12 and 13). Having the injection site closer to the narrowest nozzle cross section, the shock wave now interacts

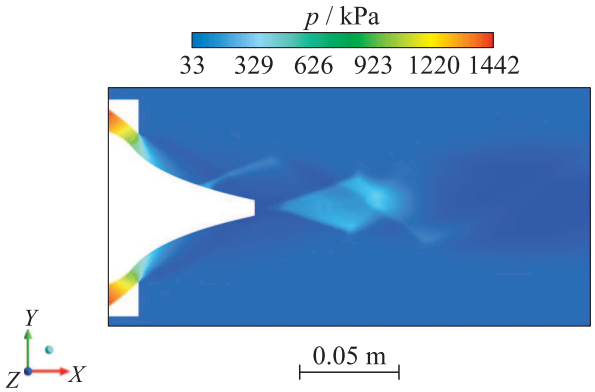

Figure 12 The CFD simulation: pressure distribution with 60 percent injection [22]

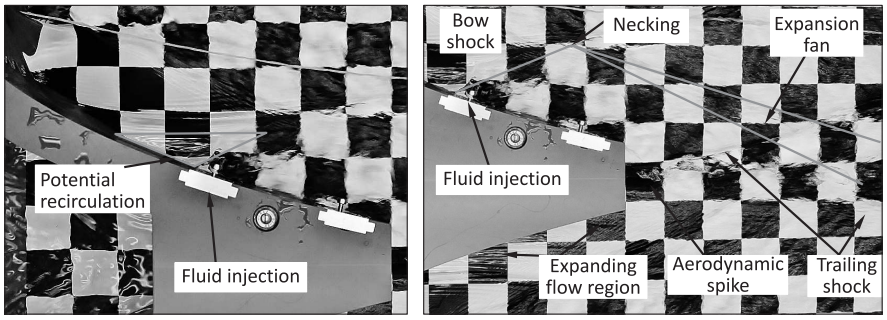

Figure 13 Experiment: (*a*) recirculation area and (*b*) flow phenomena of an overexpanded flow with 60 percent injection

directly with the expanding primary flow. As a result, a clearly visible unilateral necking is formed at the position where the bow shock meets the shear layer of the main flow, even at a minimal secondary mass flow [22]. Consequently, a new expansion region is formed starting from the necking point. This region reaches the high-pressure region behind the trailing shock and proceeds downstream as a new shock wave. This shock wave gets reflected on the opposing boundary of the free-stream and propagates further within the exhaust gas flow in the CFD-simulation. In the shallow water experiment, this shock wave is no longer noticeable after the reflection on the opposing boundary. Overall, the flow field gets much more influenced by the injection at the 60 percent position injection site compared to the downstream located injection site at 90% considered above.

5 SUMMARY AND FUTURE PERSPECTIVE

In this paper, shallow water experiments conducted for the verification of flow phenomena found in a previously realized numerical flow simulation are presented. Ensuing from the fluid model of this simulation, a shallow water model has been derived, manufactured, and tested in the described test bed. An extensive analysis of the flow phenomena in the water channel, a water surface map of the overexpanded, undeflected aerospike flow, and the comparison of the results with the simulation yield the verification of the simulation and encourage to continue further research. With an automatic traversing and surface measurement, full surface maps of more flow situations, e. g., adapted and underexpanded but essentially with secondary injection, are mandatory. Furthermore, a full spike or a completely different aerospike nozzle contour could be analyzed. In the second step, the present authors plan to continue this research in a supersonic wind tunnel, in which the pressure on the spike surface and the obtained side-forces could be measured.

ACKNOWLEDGMENTS

We appreciate the help and support of Dr.-Ing. Frank Rüdiger, Senior Researcher at the Chair of Fluid Mechanics, TU Dresden, who supported us to develop the nozzle model and provided the shallow water channel; Christiana Sperling and Rolf Rostalski for the model fabrication; and Michael Flach for supporting us during the measurements.

REFERENCES

1. Lee, C. C. 1963. FORTRAN programs for plug nozzle design. Technical note R-41.
2. Angelino, G. 1964. Performance methode for plug nozzle design. *AIAA J.* 2(10):1834–1835.
3. Hagemann, G., H. Immich, and M. Terhardt. 1998. Flow phenomena in advanced rocket nozzles — the plug nozzle. *AIAA/ASME/SAE/ASEE Joint Propulsion Conference and Exhibit*. Vol. 34.
4. Hagemann, G., H. Immich, T. V. Nguyen, and G. E. Dumnov. 1998. Advanced rocket nozzles. *J. Propul. Power* 14(5):620–634.
5. Korte, J. J. 2000. Parametric model of an aerospike rocket engine. AIAA Paper No. 2000-1044.
6. Kraiko, A. N., and N. I. Tillyayeva. 2000. Optimal profiling of the supersonic part of a plug nozzle contour. *Fluid Dyn.* 35(6):945–955.
7. Onofri, M., F. Nasuti, M. Calabro, G. Hagemann, H. Immich, P. Sacher, and P. Reijasse. 2002. Plug nozzles: Summary of flow features and engine performance. AIAA Paper No. 2002-0584.

8. Besnard, E., H. H. Chen, and T. Mueller. 2002. Design, manufacturing and test of a plug nozzle engine. AIAA Paper No. 02-4038.
9. Besnard, E., and J. Garvey. 2004. Aerospike engine for nanosat and small launch vehicles (nlv/slv). AIAA Paper No. 2004-6005.
10. Nazarinia, M., A. Naghib-Lahouti, and E. Tolouei. 2005. Design and numerical analysis of aerospike nozzles with a different plug shapes to compare their performance with a conventional nozzle. *11th Australian Aerospace Congress (International)* Vol. 11. 22 p.
11. Naghib-Lahouti, A., and E. Tolouei. 2006. Investigation of the effect of base bleed on thrust performance of a truncated aerospike nozzle in off-design conditions. *ECCOMAS CFD*.
12. Zebbiche, T., and Z. Youbi. 2006. Supersonic two-dimensional plug nozzle conception at high temperature. *Emir. J. Eng. Res.* 11(1):77–89.
13. Eilers, S. D., M. D. Wilson, D. S. A. Whitmore, and Z. W. Perterson. 2010. Analytical and experimental evaluation of aerodynamic thrust vectoring on an aerospike nozzle. AIAA Paper No. 2010-6964.
14. Erni, N. M. 2011. Closed-loop attitude control using fluid dynamic vectoring on an aerospike nozzle. PhD Diss. 112 p.
15. Propst, M., J. Sieder, C. Bach, and M. Tajmar. 2014. Numerical analysis on an aerodynamically thrust-vectored aerospike nozzle. *63rd Deutscher Luft- und Raumfahrtkongress*.
16. Dinkelacker, H.-R. 1959. Experimentelle Verfolgung zweidimensionaler instationärer Gasströmungen auf Grund der Gas-Flachwasser-Analogie. *Verlag Leemann Zürich*.
17. Eilers, S. D., M. D. Wilson, S. A. Whitmore, and Z. W. Peterson. 2012. Side-force amplification on an aerodynamically thrust-vectored aerospike nozzle. *J. Propul. Power* 28(4):811–819.
18. Albring, W. 1966. Angewandte Strömungslehre. *Verlag Theodor Steinkopff. Dresden*. Vol. 3. 380 p.
19. Trippmacher, H. 1976. Projekt einer Wasserfließrinne für Forschungsaufgaben. TU Dresden, Inst. f. Strömungsmechanik, Diplomarbeit D905.
20. Deyound, T. L. 1960. A simplified method for plug nozzle design. Technical Memorandum No. 140.
21. Sieder, J., C. Bach, M. Nürmberger, N. Voigt, O. Przybilski, and M. Tajmar. 2014. Proceedings of the SMART Rockets Project: Design development and first measurement results of a 500 N ethanol/LOx combustion chamber. *63rd Deutscher Luft- und Raumfahrtkongress*.
22. Propst, M. 2014. Numerical analysis on an aerodynamically thrust-vectored aerospike nozzle. TU Dresden, Inst. f. Luft- und Raumfahrttechnik, Diplomarbeit ILR-RSN DA 13-18.
23. Hall, J. N. 2011. Optimized dual expander aerospike rocket. Air University, Department of Aeronautics and Astronautics. Master Thesis.
24. Waidmann, W. 1991. Numerische und experimentelle Untersuchungen zur Schubvektorsteuerung durch Sekundärinjektion. *Forschungsbericht/Deutsche Forschungsanstalt für Luft- und Raumfahrt, Wiss. Berichtswesen des DLR*.